Local Extremum Constrained Total Variation Model for Natural and Hyperspectral Image Non-Blind Deblurring

Lan Li, Meiping Song, *Member, IEEE*, Qiang Zhang, *Member, IEEE*, Yushuai Dong, Yulei Wang, *Member, IEEE*, and Qiangqiang Yuan, *Member, IEEE*

Abstract— Blurring and noise degrade the performance of image processing. To mitigate this effect, various regularization-based deblurring methods have been proposed. Total variation regularization is widely used owing to its excellent ability in preserving the salient edges, but it also tends to smooth the image details. In this paper, we propose a local extremum-constrained total variation (LECTV) framework for image deblurring. In the developed deblurring framework, we integrate prior knowledge of the dark channel with the structural features of the image into a single regularization term. Furthermore, unlike most existing methods that focus on the overall sparsity of the dark channel, the defined regularization term allows for a pixel-wise adaptive description of the image to restore its inherent spatial texture structure. Finally, a majorization-minimization-based method is designed to solve the developed LECTV framework. Experimental results on natural and hyperspectral images show that the designed framework exhibits excellent performance in removing multiple types and degrees of blurring. Extensive evaluations also further show its superiority compared to other advanced methods.

Index Terms— Non-blind image deblurring, hyperspectral image (HSI), local extremum constraints, total variation (TV).

I. Introduction

IMAGE deblurring is an inverse problem in computer vision and image processing filed. The ill-posed nature poses the main challenge for these kinds of problems. In the linear observation degradation model, the degradation process can be formulated as the convolution of clear image $\mathbf{X}$ and blur kernel $\mathbf{H}$:

$$\mathbf{Y} = \mathbf{X} \otimes \mathbf{H} + \mathbf{n} \tag{1}$$

where $\mathbf{Y}$ represents the degraded image, $\mathbf{n}$ is the noise, and $\otimes$ is the convolution operation. Depending on the availability of $\mathbf{H}$, the above problem is categorized as non-blind deblurring or blind deblurring. In this paper, we focus on non-blind image deblurring, a case where the blur kernel is assumed to be known and spatially invariant. Its main task is to estimate the latent sharp version from degraded image and blur kernel. The problem is ill-posed because noise corrupts the blurred image and band-limited kernel, making the solution not unique [1], [2], [3]. This makes it difficult to estimate the corresponding sharp version from the blurred observation, even if the blur kernel is known.

Wiener filtering [4] and Bayesian-based Lucy-Richardson filtering [5] are both classical and popular filters for image deblurring. Furthermore, many variants have been developed for better simulation and lower computational costs. To effectively suppress ringing artifacts and restore images, researchers have proposed modeling strategies including low-rank or sparse prior [6], [7], [8], [9], [10], [11], [12], [13], gradient or intensity prior [14], [15], natural image statistics [3], [16], [17], sparse representation [18], [19], [20], and total variation (TV) regularization [21], [22], etc.

Recently, the TV model is widely used in image restoration due to its piecewise smoothing capability. Its excellent performance has been demonstrated in many works, such as deblurring [23], [24], [25], denoising [26], [27], [28], [29], and compressed sensing [30], [31]. Qin et al. [32] proposed an image deconvolution method based on shearlet transform and fractional order TV. Based on [32], Chowdhury et al. [24] developed a fractional-order TV to simultaneously remove blur and Poisson noise. Ren et al. [23] investigated a novel derivative space-based reformulation algorithm for TV-based image restoration by using an efficient derivative alternating direction method of multipliers (ADMM). These methods exploit the piecewise smooth property of the TV model to efficiently recover structural features in images. However, they neglect the intricate details within the images. To efficiently restore the image, Tang et al. [22] decomposed the degradation image into three parts: salient edges, details, and constant regions. Then, the TV model was applied to the salient edges and constant regions, while the non-local TV model was applied to the details. TV-based image restoration with linear filtering and soft thresholding performs was developed in [33]. It could be considered as an effective first-order algorithm for processing images of relatively large sizes. Chen et al. [34] solved the problem of nonlinear image restoration based on TV by an

objective function containing the nonlinear least-squares fitting term and TV regularization. An extending primal-dual hybrid gradient (E-PDHG) method combined with TV regularization was proposed for Prestack Seismic image deblurring [35]. By combining the normalized TV term with sparse prior knowledge of the blur kernel, Xie et al. [36] proposed a variational framework for underwater image dehazing and deblurring. In addition, TV-based model deblurring was also developed for hyperspectral image (HSI). Considering the spectral correlation between adjacent bands, Fang et al. [37] proposed a non-blind deconvolution method for HSI based on spectral-spatial TV (SSTV) model and explicit non-negative constraints. Similarly, SSTV achieved promising results in preserving salient structures in HSI, while it lacked proper attention to finer details and textures. The aforementioned studies demonstrate the effectiveness of the TV model in image restoration. However, it also tended to smooth out details while preserving salient edges in the image.

Recently, deep learning-based (DL-based) methods have been widely used for deblurring tasks [38], [39], [40], [41], [42], [43]. Xie et al. [41] proposed to learn optimal parameters for regularization adaptively based on TV deep networks, which used deep learning and prior knowledge to compute regularization parameters. It can automatically update parameters and avoid complex computations. By utilizing spectral and spatial restorers, [44] proposed to address single-image deblurring problems with a local adaptive channel attention module based on the spectral-spatial network. To connect MAP and deep model, [45] proposed two generative networks to model the deep priors of both the latent image and blur kernel, and developed an unconstrained neural optimization solution to blind deblur. In [46], Zamir et al. aimed to balance spatial details and high-level contextual information in image restoration and proposed a novel collaborative design for multi-stage progressive image restoration. Chen et al. [47] designed a non-blind image deblur deep learning method that utilized an untrained deep neural network to recover images without any external training data containing ground-truth images. Although DL-based methods can achieve satisfactory results in some blurred or noise-degraded scenarios, the complexity and variability of blur types or degrees make it unrealistic to use only a single trained network to cover all types of blurred images.

The dark channel prior (DCP) has proved useful for recovering details in the degraded image. Based on the observation that dark channel of outdoor haze-free images is almost zero, He et al. [48] proposed dark channel prior for outdoor image dehazing. Afterward, research scholars developed it for various image restoration tasks (e.g., dehazing [49], [50], underwater image restoration [51], [52]) and achieved attractive results. In previous studies [53], [54], [55], dark channel was applied to blind deblurring and performed well. Pan et al. [53] found that for natural images, most values (not all) of the dark channel as zero elements in clear images, while that of blurred images are mostly non-zero, i.e., the dark channel of clear images is sparser. They derived the properties of the blurring (convolution) operation and explained this phenomenon as the fact that the weighted sum of pixels in the local patch is larger than the minimum one, i.e. convolution increases the value of dark pixels. Based on this finding, they introduced an L_0-regularization to minimize the dark channel of the recovered image. Yan et al. [56] utilized both bright channel prior and DCP, called extreme channel prior, for deblurring operation. Ge et al. [54] applied L_1-norm to the non-linear channel (NLC) as a prior to clean images, making NLC prior to clean images rather than blurred images. All of these works made use of the property that dark channel in clear images is sparser than blurred images, removing blur from the degraded image to some extent. However, these studies focus on the overall properties of the image and do not take into account the specific situation of each pixel in the image.

Although recent research has reported more results based on the TV model, DCP, or the joint TV model and DCP for image deblurring, such as the application in recovering remote sensing images as discussed in [57] and [58], which introduced the DPC for deblurring HSI, in conjunction with the TV regularizer based on L_0 and L_1. On the one hand, while these methods aim to exploit the advantages of both techniques, they often treat the DCP or TV model merely as a separate regularization term to characterize the properties of the original image. On the other hand, these methods generally focus on leveraging the sparsity of DCP, they characterize the overall properties of the image rather than considering them pixel-wise. In this paper, we propose a novel approach: a pixel-wise adaptive constrained TV model. This model integrates the TV model with prior knowledge of blurred images into a single regularization term, allowing for a more comprehensive characterization of image texture at a per-pixel level.

The contributions of this paper are summarized as follows:

1) This paper proposes a robust image deblurring framework based on a local extremum-constrained TV (LECTV) model. The proposed framework only contains the trade-off parameter λ, the constrained TV term, and the fidelity term, which avoids the interaction and influence among parameters.

2) With the aid of the prior knowledge of blurred images, we develop a novel per-pixel adaptive constraint strategy, which can effectively recover details and preserve salient edge information of images by characterizing each pixel of the image.

3) An iterative optimization algorithm based on majorization-minimization is devised to derive and solve the proposed LECTV. The proposed method can remove multiple types and degrees of blur while suppressing slight noise.

II. RELATED METHODS

A. Maximum a Posterior Framwork

In recent years, maximum a posteriori framework (MAP) estimation theory has received increasing attentions and been also used to solve many image processing problems, such as image denoising [59], [60], [61], super-resolution [62], and deblurring [14], [41]. Based on the MAP estimation theory, for a clean image $\mathbf{X} \in \mathbb{R}^{MN \times B}$ with a spatial size of $M \times N$

and B bands, a given blurred and noisy image $\mathbf{Y} \in \mathbb{R}^{MN \times B}$ can be represented by the following image deblurring model:

$$\mathbf{X} = \arg \min L(\mathbf{X}) \tag{2}$$

$$L(\mathbf{X}) = \|\mathbf{Y} - \mathbf{HX}\|^2 + \lambda R(\mathbf{X}) \tag{3}$$

where $R(\mathbf{X})$ is the regularization term, which gives the prior of the original clean image. λ represents the corresponding weight of the regularization term.

B. Image Deblurring TV-Based Model

The TV regularization term has received extensive attentions in image restoration work due to its ability in modeling piecewise smooth image. Rudin [63] first used the TV model to solve the problem of image denoising. For a gray-level image, the basic TV model is defined as follows:

$$\text{TV}(\mathbf{X}) = \sum_{i=1}^{MN} \sqrt{\left(\nabla_i^h \mathbf{X}\right)^2 + \left(\nabla_i^v \mathbf{X}\right)^2} \tag{4}$$

where ∇_i^h and ∇_i^v are linear operators corresponding to the horizontal and vertical first-order differences at pixel i, respectively.

If we incorporate the TV model into the regularization model in (3), the TV-based deblurring can be expressed as:

$$L(\mathbf{X}) = \|\mathbf{Y} - \mathbf{HX}\|^2 + \lambda \sum_{i=1}^{MN} \sqrt{\left(\nabla_i^h \mathbf{X}\right)^2 + \left(\nabla_i^v \mathbf{X}\right)^2}. \tag{5}$$

Adding up the TV model of each band is the most straightforward way to extend the gray-level image TV model (4) to multi-spectral images or HSI. Then, a hyperspectral TV (HTV) model can be derived as below:

$$\text{HTV}(\mathbf{X}) = \sum_{j=1}^{B} \text{TV}\left(\mathbf{X}_j\right) \tag{6}$$

where $\mathbf{X} = \left[\mathbf{X}_1, \ldots, \mathbf{X}_j, \ldots, \mathbf{X}_B\right]$ is a HSI, $\mathbf{X}_j$ represents the j-th band of the HSI. However, the gradients in different bands may be inconsistent since different objects have different reflections for specific spectral bands in HSI. To some extent, these differences provide additional complementary information. Thus, the TV model of HSI can be described as [64]:

$$\text{SSTV}(\mathbf{X}) = \sum_{i=1}^{MN} \sum_{j=1}^{B} \sqrt{\left[\left(\nabla_i^h \mathbf{X}\right)^2 + \left(\nabla_i^v \mathbf{X}\right)^2 + \left(\nabla_i^s \mathbf{X}\right)^2\right]_j} \tag{7}$$

where ∇_i^s represents a first-order difference linear operator in the spectral direction. Substituting the SSTV model (7) into (3), it follows

$$L(\mathbf{X}) = \|\mathbf{Y} - \mathbf{HX}\|^2$$
$$+ \lambda \sum_{i=1}^{MN} \sum_{j=1}^{B} \sqrt{[\left(\nabla_i^h \mathbf{X}\right)^2 + \left(\nabla_i^v \mathbf{X}\right)^2 + \left(\nabla_i^s \mathbf{X}\right)^2]_j}. \tag{8}$$
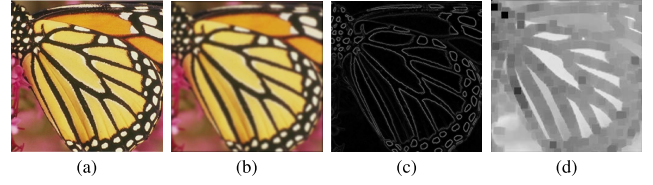

Fig. 1. The relationship between correlation values of the local minimum pixel and spatial structure of blurred image. (a) Clear, (b) Blurred, (c) Gradient of (a), (d) Correlation values of local minimum pixel.

III. PROPOSED LOCAL EXTREMUM CONSTRAINED TOTAL VARIATION MODEL

A. Constraint Based on Blur Prior

For image $\mathbf{X}$, the dark channel [48] is mainly used to describe the minimum value in the local neighborhood of the image. Here, it has been further generalized to multi-spectral and HSI, which is defined as follows:

$$\text{P}(\mathbf{X})(p) = \min_{q \in \mathcal{N}(p)} \left\{ \min_{j \in \{1, \ldots, B\}} \mathbf{X}^j(q) \right\} \tag{9}$$

where p and q represents the position of the pixel. $\mathcal{N}(p)$ represents the image patch centered on p. $\mathbf{X}_j$ represents the j-th band of image $\mathbf{X}$. If $\mathbf{X}$ is a grayscale image, it has $\min_{j \in \{1, \ldots, B\}} \mathbf{X}^j(q) = \mathbf{X}^j(q)$.

In the previous works, the sparsity of dark channels is used as priors. Unlike them, our proposed method is developed based on the fact that the dark channel is defined by the minimum pixel of local neighborhood, which can reflect the structural information of image. From Fig. 1, it gets the connection between the dark channel of the blurred image and the spatial structure. For example, Fig. 1(d) is the correlation of the minimum pixels, which reflects the structural information in Fig. 1(c) to some extent. Therefore, it takes the correlation value of the minimum pixel as a constraint to enhance the spatial structure information of the image.

B. Local Extremum Constrained Total Variation Model

This subsection presents how to implement non-blind image deblurring with the constrained TV model. Firstly, we define pixel-wise adaptive constraints based on the prior knowledge of the blurred image, which can more comprehensively reflect the image information including salient structures and fine textures. Next, it introduces that the defined constraint strategy is integrated into the traditional TV model to construct the constrained TV model. On the one hand, the constrained TV model enhances the spatial texture information in the image. On the other hand, the minimum value in the spectral dimension can reduce the influence of noise on the target to some extent. Then, the proposed constrained model is applied to natural and hyperspectral images. For convenience, the proposed methods are denoted as $\text{LECTV}_{\text{CTV}}$ and $\text{LECTV}_{\text{CHTV}}$, respectively. The constrained TV models are defined as:

$$\text{LECTV}_{\text{CTV}}(\mathbf{X})$$
$$= \sum_{i=1}^{MN} \sqrt{\mathbf{C}_{0_i} \left[\left(\nabla_i^h \mathbf{X}\right)^2 + \left(\nabla_i^v \mathbf{X}\right)^2 \right]} \tag{10}$$

$$\text{LECTV}_{\text{CHTV}}(\mathbf{X})$$

$$= \sum_{i=1}^{MN} \sum_{j=1}^{B} \sqrt{\mathbf{C}_{0_i} \left[\left(\nabla_i^h \mathbf{X}\right)^2 + \left(\nabla_i^v \mathbf{X}\right)^2 + \left(\nabla_i^s \mathbf{X}\right)^2 \right]_j} \quad (11)$$

Based on the local minimum, the constraint matrix $\mathbf{C}_0(i)$ is defined as

$$\mathbf{C}_0(i) = \varepsilon \sqrt{(\mathbf{C}(i))} \quad (12)$$

where ε is a constant that adjusts the range of values of the constraint $\mathbf{C}_0$. $\mathbf{C}$ is the local minimum value of the image, and its definition can be described as:

$$\mathbf{C}(i) = \begin{cases} \text{P}(\mathbf{X}_0)(i), & \text{P}(\mathbf{X}_0)(i) > 0 \\ \tau, & \text{otherwise} \end{cases} \quad (13)$$

where $\text{P}(\mathbf{X}_0)$ is given in (9) and τ is a positive constant set as $\tau = 10^{-6}$ in this paper.

Incorporating the $\text{LECTV}_{\text{CHTV}}$ model (11) into (3), the proposed $\text{LECTV}_{\text{CHTV}}$ method for HSI deblurring can be expressed as:

$$L(\mathbf{X}) = \|\mathbf{Y} - \mathbf{HX}\|^2$$
$$+ \lambda \sum_{i=1}^{MN} \sum_{j=1}^{B} \sqrt{\mathbf{C}_{0_i} \left[\left(\nabla_i^h \mathbf{X}\right)^2 + \left(\nabla_i^v \mathbf{X}\right)^2 + \left(\nabla_i^s \mathbf{X}\right)^2 \right]_j} \quad (14)$$

where the first fidelity term enforces similarity between $\mathbf{Y}$ and $\mathbf{HX}$, and the second one is the constrained TV regularization term. In (14), the $\text{LECTV}_{\text{CHTV}}$ model considers the multi-band structure of HSI, which can produce more reliable results than deconvolution by each band alone. Similarly, combining (10) with (3), the proposed $\text{LECTV}_{\text{CTV}}$ method is rendered as:

$$L(\mathbf{X}) = \|\mathbf{Y} - \mathbf{HX}\|^2 + \lambda \sum_{i=1}^{MN} \sqrt{\mathbf{C}_{0_i} \left[\left(\nabla_i^h \mathbf{X}\right)^2 + \left(\nabla_i^v \mathbf{X}\right)^2 \right]}. \quad (15)$$

As illustrated in Fig. 2, the framework visually depicts how LECTV utilizes the prior information of the blurred image as a constraint for image restoration. Specifically, LECTV constructs a constraint matrix by utilizing the pixel information and the prior knowledge reflected in the blurred image itself. Subsequently, it employs pixel-wise to constrain the gradient map, forming a local extremum-constrained TV model. Further details will be provided in the subsequent subsections.

C. Derivation of Model Solving

Let $\mathbf{X}^{(k)}$ denote the image at the k-th iteration. The function $F(\mathbf{X} \mid \mathbf{X}^{(k)})$ satisfies:

$$F(\mathbf{X}^{(k)} \mid \mathbf{X}^{(k)}) = L(\mathbf{X}^{(k)}) \quad (16)$$

$$L(\mathbf{X}) \le F(\mathbf{X} \mid \mathbf{X}^{(k)}), \quad \mathbf{X} \ne \mathbf{X}^{(k)} \quad (17)$$

where $F(\mathbf{X} \mid \mathbf{X}^{(k)})$ is a function of $\mathbf{X}$ and serves as an upper bound for $L(\mathbf{X})$. Assume that $\mathbf{X}^{(k+1)}$ is obtained from the following equation:

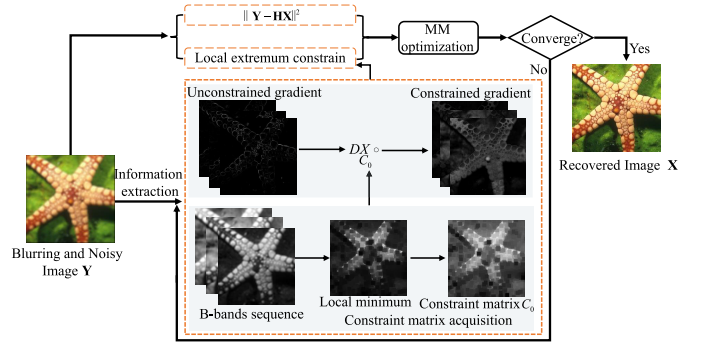$$\mathbf{X}^{(k+1)} = \arg\min_{\mathbf{X}} F(\mathbf{X} \mid \mathbf{X}^{(k)}). \quad (18)$$

Fig. 2. Framework of the proposed LECTV image deblurring method.

Then, it follows

$$L\left(\mathbf{X}^{(k+1)}\right) \le F\left(\mathbf{X}^{(k+1)} \mid \mathbf{X}^{(k)}\right) \le F\left(\mathbf{X}^{(k)} \mid \mathbf{X}^{(k)}\right) = L\left(\mathbf{X}^{(k)}\right). \quad (19)$$

In this paper, instead of solving each linear system exactly, we only reduce the relevant quadratic function. According to [65], conjugate gradient (CG) algorithms can be employed for implementation. Since (14) is already quadratic, for (11), according to the following facts:

$$\sqrt{a} \le \sqrt{a_0} + \frac{1}{2\sqrt{a_0}}(a - a_0) \quad (20)$$

for any $a \ge 0$ and $a_0 \ge 0$, the above equation holds. The definition of the function F_{CHTV} is presented in (21), as shown at the bottom of the next page, where $\mathbf{C}_0 = \mathbf{C}(\mathbf{X}^0)$ is a constant matrix. For any $\mathbf{X}$, $\mathbf{X}^{(k)}$ satisfies $F_{\text{CHTV}}(\mathbf{X} \mid \mathbf{X}^{(k)}) \ge \text{CHTV}(\mathbf{X})$ and the equality if and only if $\mathbf{X} = \mathbf{X}^{(k)}$. Then, (21) can be rewritten as:

$$F_{\text{CHTV}}\left(\mathbf{X} \mid \mathbf{X}^{(k)}\right)$$

$$= \frac{1}{2} \sum_{i=1}^{MN} \sum_{j=1}^{B} \frac{\mathbf{C}_{0_i} \left(\nabla_i^h \mathbf{X}\right)_j^2}{\sqrt{\mathbf{C}_{0_i} \left[\left(\nabla_i^h \mathbf{X}^{(k)}\right)^2 + \left(\nabla_i^v \mathbf{X}^{(k)}\right)^2 + \left(\nabla_i^s \mathbf{X}^{(k)}\right)^2 \right]_j}}$$

$$+ \frac{1}{2} \sum_{i=1}^{MN} \sum_{j=1}^{B} \frac{\mathbf{C}_{0_i} \left(\nabla_i^v \mathbf{X}\right)_j^2}{\sqrt{\mathbf{C}_{0_i} \left[\left(\nabla_i^h \mathbf{X}^{(k)}\right)^2 + \left(\nabla_i^v \mathbf{X}^{(k)}\right)^2 + \left(\nabla_i^s \mathbf{X}^{(k)}\right)^2 \right]_j}}$$

$$+ \frac{1}{2} \sum_{i=1}^{MN} \sum_{j=1}^{B} \frac{\mathbf{C}_{0_i} \left(\nabla_i^s \mathbf{X}\right)_j^2}{\sqrt{\mathbf{C}_{0_i} \left[\left(\nabla_i^h \mathbf{X}^{(k)}\right)^2 + \left(\nabla_i^v \mathbf{X}^{(k)}\right)^2 + \left(\nabla_i^s \mathbf{X}^{(k)}\right)^2 \right]_j}}$$

$$+ \text{K}\left(\mathbf{X}^{(k)}\right) \quad (22)$$

where $\text{K}(\mathbf{X}^{(k)})$ is a constant independent of $\mathbf{X}$. Therefore, $F_{\text{CHTV}}(\mathbf{X} \mid \mathbf{X}^{(k)})$ provides a quadratic upper bound on $\text{CHTV}(\mathbf{X})$. Define $\mathbf{w}^{(k)} = \left\{ w_i^{(k)}, i = 1, \dots, MN \right\}$ with

$$w_i^{(k)} = \frac{1}{\sqrt{\mathbf{C}_{0_i} \left[\left(\nabla_i^h \mathbf{X}^{(k)}\right)^2 + \left(\nabla_i^v \mathbf{X}^{(k)}\right)^2 + \left(\nabla_i^s \mathbf{X}^{(k)}\right)^2 \right]_j}} \quad (23)$$

Then, (22) can be rewritten as:

$$
\begin{aligned}
&F_{\text{CHTV}}\left(\mathbf{X} \mid \mathbf{X}^{(k)}\right) \\
&= \frac{1}{2} \sum_{i=1}^{MN}\left[\left[\mathbf{D}^s\mathbf{X}\right]_i^2\left(\mathbf{C}_{0_i}\mathbf{w}_{j,i}\right)\right] + \mathrm{K}\left(\mathbf{X}^{(k)}\right) \\
&\quad + \frac{1}{2}\sum_{i=1}^{MN}\left[\left[\mathbf{D}^h\mathbf{X}\right]_i^2\left(\mathbf{C}_{0_i}\mathbf{w}_{j,i}\right) + \left[\mathbf{D}^v\mathbf{X}\right]_i^2\left(\mathbf{C}_{0_i}\mathbf{w}_{j,i}\right)\right]
\end{aligned}
\quad (24)
$$

with $\mathbf{D}^h$, $\mathbf{D}^v$, and $\mathbf{D}^s$ being the first-order differences operators along the X-axis, Y-axis, and Z-axis, respectively.

In addition, define a diagonal matrix

$$
\boldsymbol{\Lambda}^{(k)} = \operatorname{diag}\left(\mathbf{C}_{0_i}\mathbf{w}^{(k)}\right). \quad (25)
$$

With the aid of (25), F_{CHTV} can be rewritten as:

$$
F_{\text{CHTV}}\left(\mathbf{X} \mid \mathbf{X}^{(k)}\right) = \mathbf{X}^T\mathbf{D}^T\Upsilon^{(k)}\mathbf{D}\mathbf{X} + \mathrm{K}\left(\mathbf{X}^{(k)}\right) \quad (26)
$$

with $\mathbf{D} = [(\mathbf{D}^h)^T(\mathbf{D}^v)^T(\mathbf{D}^s)^T]^T$ and $\Upsilon^{(k)} = \operatorname{diag}\left(\boldsymbol{\Lambda}^{(k)}, \boldsymbol{\Lambda}^{(k)}, \boldsymbol{\Lambda}^{(k)}\right)$. Substituting λF_{CHTV} into (14), it yields

$$
\begin{aligned}
&F\left(\mathbf{X} \mid \mathbf{X}^{(k)}\right) \\
&= \|\mathbf{Y} - \mathbf{H}\mathbf{X}\|^2 + \lambda\mathbf{X}^T\mathbf{D}^T\Upsilon^{(k)}\mathbf{D}\mathbf{X} + \lambda\mathrm{K}\left(\mathbf{X}^{(k)}\right) \\
&= \mathbf{X}^T\left(\mathbf{H}^T\mathbf{H} + \lambda\mathbf{D}^T\Upsilon^{(k)}\mathbf{D}\right)\mathbf{X} - 2\mathbf{X}^T\mathbf{H}\mathbf{Y} + \mathrm{K}'\left(\mathbf{X}^{(k)}\right)
\end{aligned}
\quad (27)
$$

where $\mathrm{K}'\left(\mathbf{X}^{(k)}\right)$ represents a constant independent of $\mathbf{X}$.

By minimizing (27), it has

$$
\mathbf{X}^{(k+1)} = \left(\mathbf{H}^T\mathbf{H} + \lambda\mathbf{D}^T\Upsilon^{(k)}\mathbf{D}\right)^{-1}\mathbf{H}^T\mathbf{Y} \quad (28)
$$

From (28), obtaining $\mathbf{X}^{(k+1)}$ is equivalent to solving the large linear system $\mathbf{A}^{(k)}\mathbf{X} = \bar{\mathbf{Y}}$, where $\mathbf{A}$ is defined as $\mathbf{A} \equiv \mathbf{H}^T\mathbf{H} + \lambda\mathbf{D}^T\Upsilon^{(k)}\mathbf{D}$ and $\bar{\mathbf{Y}}$ is calculated as $\bar{\mathbf{Y}} = \mathbf{H}^T\mathbf{Y}$. This paper solves the problem by using the CG algorithm. LECTV iteratively updates $F\left(\mathbf{X} \mid \mathbf{X}^{(k)}\right)$ and ensures a reduction of $F\left(\mathbf{X} \mid \mathbf{X}^{(k)}\right)$ with respect to $\mathbf{X}$.

D. Algorithm Description

Algorithm 1 summarizes main steps to optimize and solve the LECTV-based image deblurring problem using the MM technique.

$iter$ is the iterative stop condition of the MM algorithm, and λ is the regularization parameter. Inspired by [25], we design a new adaptive λ. The new designed λ can adjust adaptively.

Algorithm 1 LECTV-Based Image Restoration

Input: Dedraded image Y
Initialization: $\mathbf{X}_0$, $iter$
  while λ iteration stopping condition not met **do**
    Compute $\mathbf{C}_0(i)$ according (12)
    Compute λ according (29) or (30)
    while MM iteration stopping condition not met **do**
      Compute matrix $\boldsymbol{\Lambda}^{(k)}$ using (23), (24), and (25)
      Compute $F\left(\mathbf{X} \mid \mathbf{X}^{(k)}\right)$ by (27)
      $\mathbf{X}^{(k+1)} := \mathbf{X}^{(k)}$
      while CG iteration stopping condition not met **do**
        $\mathbf{X}^{(k+1)} :=$ CG iteration for system $\mathbf{A}^{(k)}\mathbf{X} = \bar{\mathbf{Y}}$, initialized at $\mathbf{X}^{(k+1)}$
      end while
      $k = k + 1$
    end while
  end while
Output: The restoration result

Moreover, the definition of λ indicates that it is related to the degree of image blurring. In a grayscale image, the parameter λ is defined as

$$
\lambda^{(k)} = \frac{\rho\sigma^2}{\frac{1}{\mathbf{C}_{0_i}}\left[\left(\nabla_i^h\mathbf{X}^{(k)}\right)^2 + \left(\nabla_i^v\mathbf{X}^{(k)}\right)^2\right] + \beta} \quad (29)
$$

For a HSI, the parameter λ can be rewritten as

$$
\lambda^{(k)} = \frac{\rho\sigma^2}{\frac{1}{\mathbf{C}_{0_i}}\left[\left(\nabla_i^h\mathbf{X}^{(k)}\right)^2 + \left(\nabla_i^v\mathbf{X}^{(k)}\right)^2 + \left(\nabla_i^s\mathbf{X}^{(k)}\right)^2\right]_j + \beta} \quad (30)
$$

where $\rho = 2(\alpha + \theta MN)$; σ is the standard deviation of zero mean Gaussian noise. The values of ρ, β and θ are consistent with the comparison algorithm adaptive TV [25]. As can be seen from the above definition (29) and (30), the parameter λ is also adaptive, which does not need to be manually specified. In addition, each band of HSI has an independent value of λ, which is more applicable to the deblurring of different bands.

IV. Experiment Results Analysis

In this section, firstly, we describe the evaluation metrics, experimental setup, and datasets. Then, we provide performance evaluations of the proposed method and implement comparative experiments on multiple datasets.

$$
\begin{aligned}
F_{\text{CHTV}}\left(\mathbf{X} \mid \mathbf{X}^{(k)}\right) = \text{CHTV}\left(\mathbf{X}^{(k)}\right) &+ \frac{1}{2}\sum_{i=1}^{MN}\sum_{j=1}^{B}\frac{\mathbf{C}_{0_i}\left[\left(\nabla_i^h\mathbf{X}\right)^2 + \left(\nabla_i^v\mathbf{X}\right)^2 + \left(\nabla_i^s\mathbf{X}\right)^2\right]_j}{\sqrt{\mathbf{C}_{0_i}\left[\left(\nabla_i^h\mathbf{X}^{(k)}\right)^2 + \left(\nabla_i^v\mathbf{X}^{(k)}\right)^2 + \left(\nabla_i^s\mathbf{X}^{(k)}\right)^2\right]_j}} \\
&- \frac{1}{2}\sum_{i=1}^{MN}\sum_{j=1}^{B}\frac{\mathbf{C}_{0_i}\left[\left(\nabla_i^h\mathbf{X}^{(k)}\right)^2 + \left(\nabla_i^v\mathbf{X}^{(k)}\right)^2 + \left(\nabla_i^s\mathbf{X}^{(k)}\right)^2\right]_j}{\sqrt{\mathbf{C}_{0_i}\left[\left(\nabla_i^h\mathbf{X}^{(k)}\right)^2 + \left(\nabla_i^v\mathbf{X}^{(k)}\right)^2 + \left(\nabla_i^s\mathbf{X}^{(k)}\right)^2\right]_j}}
\end{aligned}
\quad (21)
$$

A. Evaluation Metric and Experimental Setting

The quality of the restoration image is very important for subsequent processing, but it is difficult to judge directly by visual effects. Therefore, in order to give a comprehensive evaluation, the experimental results on RGB images and HSI are evaluated quantitatively and qualitatively. Peak Signal-to-Noise Ratio (PSNR) and Structural Similarity (SSIM) are used for quantitative metrics of natural images. PSNR, SSIM, Spectral Angle Mapper (SAM) and Erreur Relative Globale Adimensionnelle de Synthese (ERGAS) are used on HSI. Among them, PSNR and SSIM values are used to evaluate the spatial quality of the image, with larger values corresponding to a better quality of the restoration image. SAM and ERGAS values are used to measure the spectral quality of the restoration image, with smaller values corresponding to a better quality of the restoration image.

The test datasets consist of three nature image datasets, and HSI datasets. In detail, natural image datasets contain: the dataset in [66], labeled as Dataset1, with 20 grayscale images; the dataset in [67], labeled as Dataset2, with 9 color images and 6 grayscale images; and the Berkeley Segmentation Dataset in [68], labeled as Dataset3, with 100 images. In experiments on HSI, CAVE dataset, Pavia University, Urban data, and Pavia City data are used to validate the effectiveness of the proposed method. To demonstrate the adaptation of LECTV under multiple degradation environments, we simulate seven different cases as follows:

1) GaussianA: $\delta = 1.6$ and $\sigma = 0.00006$ (average PSNR is 24.30dB);
2) GaussianB: $\delta = 3$ and $\sigma = 0.0001$ (average PSNR is 22.91dB);
3) GaussianC: $\delta = 5$ and $\sigma = 0.0001$ (average PSNR is 22.55dB);
4) SquareA: side size $s = 9$ and $\sigma = 0.00006$ (average PSNR is 21.48dB);
5) SquareB: side size $s = 13$ and $\sigma = 0.00006$ (average PSNR is 20.31dB);
6) MotionA: The motion kernel with a motion displacement of 20 pixels, angle with 15 degrees and $\sigma = 0.0002$ (average PSNR is 20.75dB);
7) MotionB: The motion kernel with a motion displacement of 35 pixels, angle with 45 degrees and $\sigma = 0.0002$ (average PSNR is 18.65dB);

where δ and σ denote standard deviation of Gaussian kernel and Gaussian noise, respectively. The average PSNR value is calculated by all datasets including Dataset1, Dataset2, and Dataset3.

B. Effects of Adding the Local Extremum Constraints

In this subsection, firstly, we show the gradient with or without the local extremum constraint. Then, it presents the comparison result of the TV-based algorithm and the constrained TV-based algorithm.

1) Effect on Gradient: Fig. 3 shows the unconstrained and the constrained gradient of the degraded image (the degraded image is generated by GaussianA). It can be seen that the

Fig. 3. Comparison of unconstrained and constrained gradients of degraded image. (a) Clear, (b) Blurred, (c) Unconstrained gradients of (b), (d) Constrained gradients of (b).
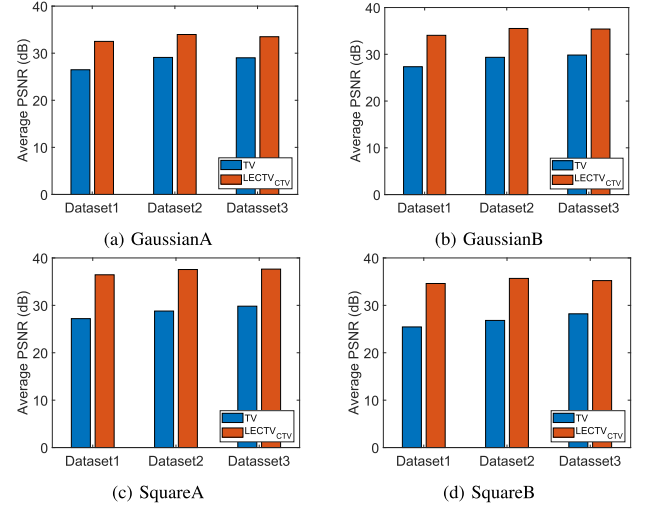

Fig. 4. The average PSNR of TV and LECTV$_{CTV}$.

unconstrained gradient (Fig. 3(c)) has less structural information, which results in smoother segmentation boundaries. On the contrary, the constrained gradient (Fig. 3(d)) has more vivid texture details and sharper boundaries. The structural information is clearer and more reliable than the unconstrained version.

2) Effect on Performance: In this subsection, the experiments are implemented to verify the effectiveness of the proposed local extremum constraint. The TV-based method [25] and the proposed constrained TV-based method are represented with TV and LECTV$_{CTV}$, respectively. The performance of the LECTV$_{CTV}$ is evaluated on Dataset1, Dataset2, and Dataset3. Herein, we select four degradation cases including GaussianA, GaussianB, SquareA, and SquareB. The average PSNR and SSIM values of the restoration results are shown in Fig. 4 and Fig. 5, respectively. It can be noticed that the indices of the LECTV model are superior to the TV model in all cases.

Fig. 6 displays the visual restoration examples in the cases of GuassianA and SquareA. It is evident that the TV-based image is still a slight blur in the local details. In contrast, the LECTV$_{CTV}$ method performs well in the finer details. Thus, it is seen that the local extremum constraint can compensate the detail information with the inherent structure of the image.

C. Experiments on Nature Images

To illustrate the superiority of the proposed method, experiments on multiple datasets are performed and compared with other competitors including hyper-laplacian prior method (HL) [69], adaptive TV deblurring algorithm [25], ADMM-C and
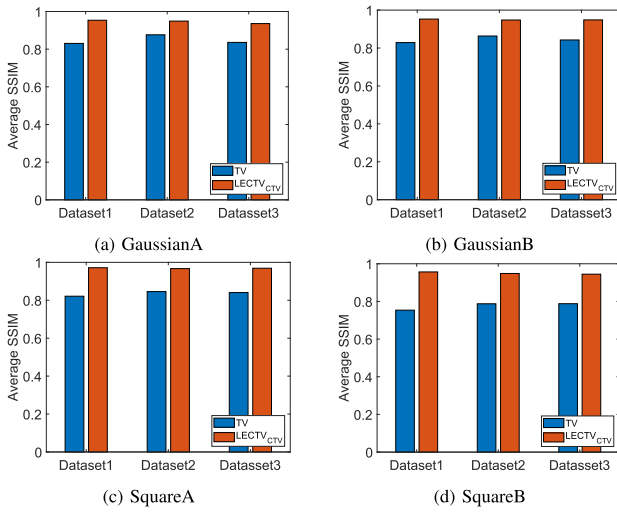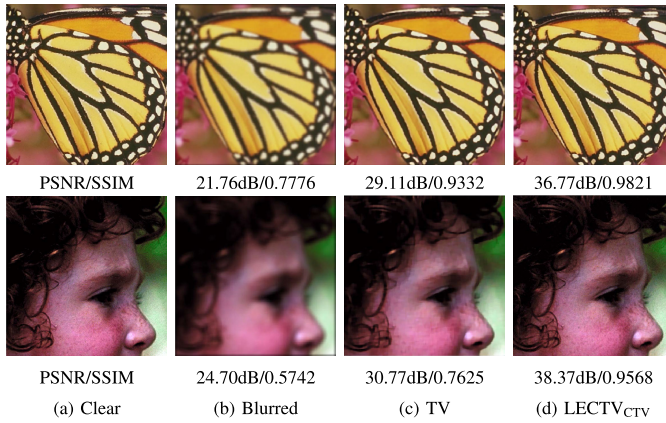
Fig. 5. The average SSIM of TV and LECTV$_{CTV}$.

Fig. 6. Visual example restored by TV and LECTV$_{CTV}$ (The first row is degenerated by GuassianA and the second row is degenerated by SquareA).

ADMM-H [23], nonlocally centralized sparse representation (NCSR) [18], cascade of shrinkage fields (CSF) [66], learning fully convolutional networks (LFCNN) [70], SelfDeblur [45], MPRNet [46], FTOAC [71] and INFWIDE [72]. To facilitate the comparison of different methods, the best values in the experiments are highlighted in bold font.

Tables I-III show the average performance (PSNR/SSIM) of different methods on Dataset1, Dataset2, and Dataset3, respectively. Firstly, in multiple datasets and degradation types, the PSNR and SSIM values of the proposed LECTV$_{CTV}$ achieve the highest performance in almost all cases, which shows the superiority of LECTV$_{CTV}$. Secondly, it is known from the experimental results on the three datasets that the performance of HL and CSF decreases significantly under the case of SquareA, SquareB, MotionA, and MotionB. The performance of ADMM-H, ADMM-C, and LFCNN are degraded in the cases of SquareA, SquareB, and MotionB. The performance of NCSR is also degraded significantly in the SquareB case. Four DL-based methods (MPRNET, SelfDeblur, FTOAC, and INFWIDE) also have significantly degraded performance on two motion blur cases (MotionA and MotionB), which reflects the limitation of the generalization ability of DL-based meth-

ods. TV-based method is also degraded under SquareB and MotionB. In contrast, the results of the proposed LECTV$_{CTV}$ achieve the stable and superior performance on different blur kernels and datasets. It also shows the robustness and effectiveness of the LECTV$_{CTV}$ algorithm. In addition, compared with the TV model, the LECTV$_{CTV}$ has better performance in different degradation cases and datasets, which illustrates the effectiveness of the proposed local extremum constrained TV model.

It is also of great significance for the performance evaluation of algorithms that the restoration results are realistic and natural. In order to visually evaluate the reliability of the restoration results, we consider three degradation cases on different images with comparisons. Figs. 7-9 display the blurred images and restoration results in the cases of GuassianA, SquareA, and MotionA, respectively. From Figs. 7-9, it gets visually that the proposed LECTV$_{CTV}$ method can always achieve better restoration results than other competitors, especially in terms of image details. Specifically, compared to other methods, the recovery results of LECTV$_{CTV}$ exhibit sharper edges and textures. This is particularly evident in selectively enlarged regions, such as the stamen of a flower and the facial features of a parrot. This indicates that LECTV$_{CTV}$ performs well in restoring the texture features for the image by incorporating both pixel information and prior knowledge of the blurred image. Furthermore, this also demonstrates that pixel-wise constraints are effective in recovering fine details of the image.

In addition, we compare the convergence of LECTV$_{CHTV}$ and TV method. Fig. 10 shows the evolution of PSNR and objective function value in the restoration process for TV and LECTV$_{CTV}$ on the Flower image (GaussianA, PSNR: 24.91dB). It is seen from the evolution graph that the LECTV$_{CTV}$ has a smaller error and a higher PSNR value than the TV-based method. As the number of iterations increases, the relative change values of LECTV's PSNR converge to 0 more quickly, which also implies that our method spends fewer iterations.

D. Experiments on Hyperspectral Images

According to the multi-band characteristics of HSI, we further extend the proposed LECTV$_{CTV}$ to LECTV$_{CHTV}$. The proposed LECTV$_{CHTV}$ considers the spectral information of HSI and utilizes the unique spectral redundancy among adjacent spectral bands, which are combined with other spectral bands to compensate for the disturbed information. Therefore, deconvolution with multiple bands can obtain more reliable results than an individual band. In this subsection, LECTV (including LECTV$_{CTV}$ and LECTV$_{CHTV}$) is tested on HSI to demonstrate the validity of the proposed method. The single-image-based HL [69], FPD [73], SSTV [37], WLRTR [74] and OLRT [75] are used to compare with the presented LECTV method. The CAVE dataset and three HSI are used to verify the superiority of the proposed method. The size of image in the CAVE dataset is 512×512 pixels with 31 spectral bands. Three HSI are composed of Pavia University ($610 \times 340 \times 103$), Urban ($307 \times 307 \times 162$) and Pavia Center ($200 \times 200 \times 191$).

TABLE I
PERFORMANCE COMPARISON OF DATASET1

Case	Index	HL	ADMM-C	ADMM-H	NCSR	CSF	LFCNN	MPRNET	SelfDeblur	FTOAC	INFWIDE	TV	LECTV$_{CTV}$
GaussianA	PSNR	24.84	25.76	25.25	<u>30.82</u>	23.51	25.56	22.93	24.05	23.12	25.33	26.48	**32.51**
	SSIM	0.7714	0.8148	0.8079	<u>0.9245</u>	0.7369	0.7930	0.6626	0.6990	0.7126	0.7111	0.8306	**0.9536**
GaussianB	PSNR	23.94	26.23	25.47	<u>31.52</u>	22.32	24.77	22.13	23.90	20.97	24.33	27.34	**34.06**
	SSIM	0.7033	0.8074	0.7894	<u>0.9141</u>	0.6586	0.7494	0.5753	0.6538	0.5222	0.6588	0.8286	**0.9527**
GaussianC	PSNR	24.24	26.73	25.85	<u>32.86</u>	22.20	25.17	22.12	25.16	20.41	24.69	28.13	**36.26**
	SSIM	0.7112	0.826	0.8049	<u>0.9318</u>	0.6528	0.7662	0.5712	0.7078	0.4681	0.6742	0.8514	**0.9687**
SquareA	PSNR	23.24	25.42	24.66	<u>32.12</u>	21.26	24.06	21.80	24.71	19.62	24.19	27.20	**36.45**
	SSIM	0.6528	0.7707	0.7493	<u>0.9262</u>	0.5864	0.7121	0.5360	0.6799	0.3766	0.6542	0.8214	**0.9716**
SquareB	PSNR	21.58	23.23	22.68	<u>29.07</u>	20.04	22.14	20.61	22.93	19.03	22.69	25.45	**34.61**
	SSIM	0.5524	0.6574	0.6359	<u>0.8694</u>	0.4923	0.5997	0.4630	0.5790	0.3345	0.5905	0.7536	**0.9566**
MotionA	PSNR	23.72	26.46	25.22	<u>35.28</u>	21.00	20.54	24.29	19.61	19.23	22.09	30.60	**36.78**
	SSIM	0.7003	0.8246	0.7959	<u>0.9524</u>	0.5991	0.6186	0.7090	0.4033	0.4435	0.6230	0.9049	**0.9616**
MotionB	PSNR	21.32	23.07	22.08	<u>33.77</u>	18.53	19.66	17.30	18.26	17.79	20.93	25.70	**35.56**
	SSIM	0.5667	0.6842	0.6503	<u>0.9293</u>	0.4442	0.5407	0.2998	0.3613	0.3378	0.5694	0.7664	**0.9494**

TABLE II
PERFORMANCE COMPARISON OF DATASET2

Case	Index	HL	ADMM-C	ADMM-H	NCSR	CSF	LFCNN	MPRNET	SelfDeblur	FTOAC	INFWIDE	TV	LECTV$_{CTV}$
GaussianA	PSNR	27.47	28.11	27.53	<u>32.28</u>	25.58	26.09	23.22	25.02	23.61	26.41	29.10	**34.97**
	SSIM	0.8347	0.8546	0.8505	<u>0.9313</u>	0.8097	0.8448	0.8092	0.8501	0.8322	0.8600	0.8763	**0.9490**
GaussianB	PSNR	26.39	28.18	27.43	<u>33.12</u>	24.27	25.36	22.93	24.74	21.69	25.45	29.35	**35.52**
	SSIM	0.7863	0.8390	0.8265	<u>0.9241</u>	0.7466	0.8068	0.7841	0.8234	0.7331	0.8304	0.8632	**0.9477**
GaussianC	PSNR	26.50	28.47	27.63	<u>34.31</u>	24.08	25.50	23.29	25.69	21.16	25.74	29.93	**37.36**
	SSIM	0.7849	0.8469	0.8322	<u>0.9367</u>	0.7370	0.8088	0.7938	0.8393	0.7033	0.8373	0.8729	**0.9624**
SquareA	PSNR	25.19	27.14	26.33	<u>32.86</u>	22.93	24.51	22.93	25.41	20.24	25.04	28.80	**37.56**
	SSIM	0.7354	0.8065	0.7881	<u>0.9175</u>	0.6754	0.7682	0.7711	0.8172	0.6416	0.8251	0.8458	**0.9670**
SquareB	PSNR	23.40	24.93	24.30	<u>29.75</u>	21.57	22.93	21.21	24.06	19.17	23.44	26.82	**35.68**
	SSIM	0.6578	0.7245	0.7042	<u>0.8608</u>	0.5974	0.6937	0.7024	0.7543	0.5889	0.7908	0.7875	**0.9484**
MotionA	PSNR	25.24	27.72	26.52	<u>35.73</u>	22.21	21.90	25.00	19.01	18.76	23.22	31.92	**38.42**
	SSIM	0.7497	0.8390	0.8163	<u>0.9435</u>	0.6636	0.6843	0.8265	0.5981	0.6103	0.8083	0.9065	**0.9541**
MotionB	PSNR	23.16	24.92	23.84	<u>34.04</u>	20.20	21.02	17.82	18.01	17.38	21.34	28.21	**37.64**
	SSIM	0.6697	0.7580	0.7299	<u>0.9168</u>	0.5657	0.6586	0.5701	0.5817	0.5488	0.7655	0.8334	**0.9458**

These datasets have also been used in HSI deblurred studies to validate the performance [12], [74], [75], [76].

The Gaussian blur kernels with standard deviations of 3 (Case A) and 5 (Case B) are used to obtain the degraded images, which are also added to the additional Gaussian noise. In order to ensure the fairness, the experimental parameters of all competitors are finely tuned based on default settings from codes of authors' individual websites or parameter ranges of these papers (especially WLRTR [74] and OLRT [75]) to achieve the optimal performance. To facilitate finding the better performance on different methods, the best and second-best values are labeled in bold and underlined, respectively.

1) Experimental Results Analysis on CAVE Dataset: The quantitative evaluation results of CAVE Dataset are shown in Table IV. From visual and quantitative evaluation metrics, it follows that both the proposed algorithm and competitors can improve the quality of degraded images. It shows that the proposed LECTV method outperforms the FPD, SSTV, HL, WLRTR, and OLRT methods in four quantification metrics. Specifically, LECTV$_{CHTV}$ acquires the best values in PSNR, SSIM, SAM, and ERGAS in Case B, while LECTV$_{CTV}$ achieves the second-best results in four metrics. In Case A, the best PSNR, SSIM, and SAM values are achieved by LECTV$_{CTV}$, and LECTV$_{CHTV}$ achieves best in ERGAS.

TABLE III
PERFORMANCE COMPARISON OF DATASET3

Case	Index	HL	ADMM-C	ADMM-H	NCSR	CSF	LFCNN	MPRNET	SelfDeblur	FTOAC	INFWIDE	TV	LECTV$_{CTV}$
GaussianA	PSNR	27.17	27.91	27.52	31.85	26.11	25.87	24.36	24.86	23.95	25.68	29.02	**33.50**
	SSIM	0.7677	0.8043	0.8009	0.9195	0.7509	0.7680	0.8174	0.8274	0.8217	0.8496	0.8359	**0.9359**
GaussianB	PSNR	26.26	27.90	27.45	33.01	25.09	25.28	23.76	24.34	22.73	24.45	29.84	**35.40**
	SSIM	0.7111	0.7864	0.7768	0.9297	0.6922	0.7217	0.7822	0.7998	0.7511	0.8158	0.8424	**0.9483**
GaussianC	PSNR	26.37	28.24	27.73	34.12	24.99	25.44	23.72	24.70	22.29	25.20	30.57	**37.00**
	SSIM	0.7111	0.8023	0.7914	0.9410	0.6882	0.7277	0.7797	0.8117	0.7266	0.8342	0.8625	**0.9615**
SquareA	PSNR	25.43	27.10	26.62	32.76	24.14	24.73	23.02	24.55	21.62	24.92	29.82	**37.64**
	SSIM	0.6655	0.7516	0.7399	0.9226	0.6390	0.6855	0.7536	0.8056	0.6882	0.8283	0.8405	**0.9690**
SquareB	PSNR	24.13	25.28	24.91	29.93	23.08	23.68	22.01	23.69	20.98	23.74	28.21	**35.22**
	SSIM	0.60	0.6596	0.6497	0.8662	0.5761	0.6230	0.7188	0.7754	0.6664	0.800	0.7879	**0.9447**
MotionA	PSNR	25.95	28.13	27.38	37.04	24.20	23.91	24.85	20.70	20.61	23.59	33.53	**37.28**
	SSIM	0.7108	0.8113	0.7960	**0.9613**	0.670	0.6885	0.8346	0.6667	0.6739	0.8189	0.9203	0.9432
MotionB	PSNR	23.93	25.41	24.72	33.64	22.17	22.57	19.11	19.93	19.41	21.90	28.76	**36.42**
	SSIM	0.6140	0.7017	0.6836	0.9238	0.5597	0.6020	0.6258	0.6653	0.6273	0.7697	0.7924	**0.9336**

(a) Blurred   (b) HL   (c) ADMM-C   (d) ADMM-H   (e) NCSR   (f) CSF   (g) LFCNN

(h) MPRNET   (i) SelfDeblur   (j) FTOAC   (k) INFWIDE   (l) TV   (m) LECTV$_{CTV}$ (n) Clear

Fig. 7. Visual examples: GuassianA.

(a) Blurred   (b) HL   (c) ADMC   (d) ADMH   (e) NCSR   (f) CSF   (g) LFCNN

(h) MPRNet   (i) SelfDeblur   (j) INFWIDE   (k) FTOAC   (l) TV   (m) LECTV$_{CTV}$ (n) Clear
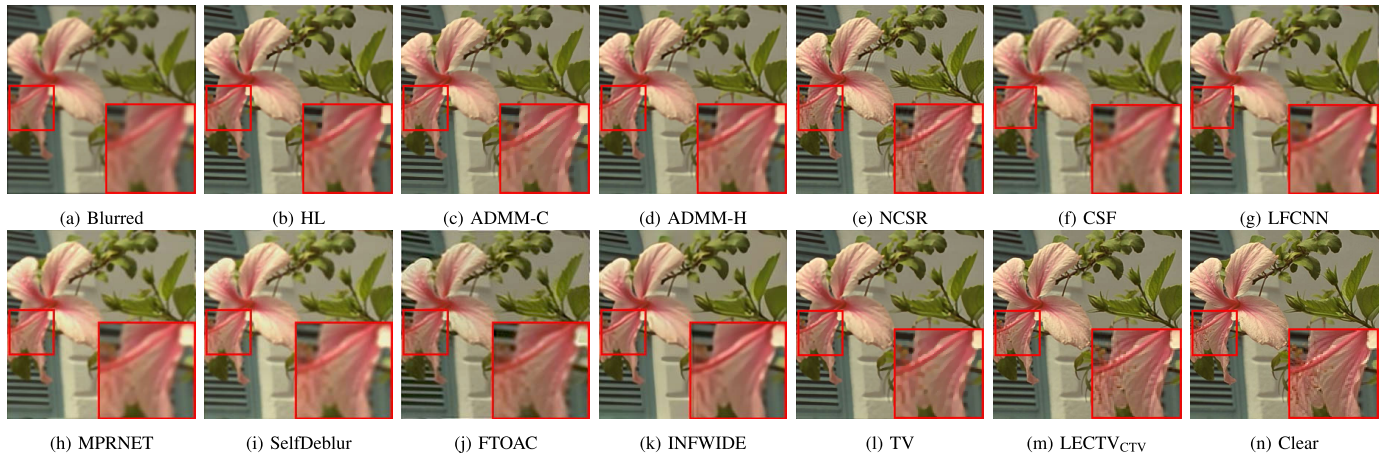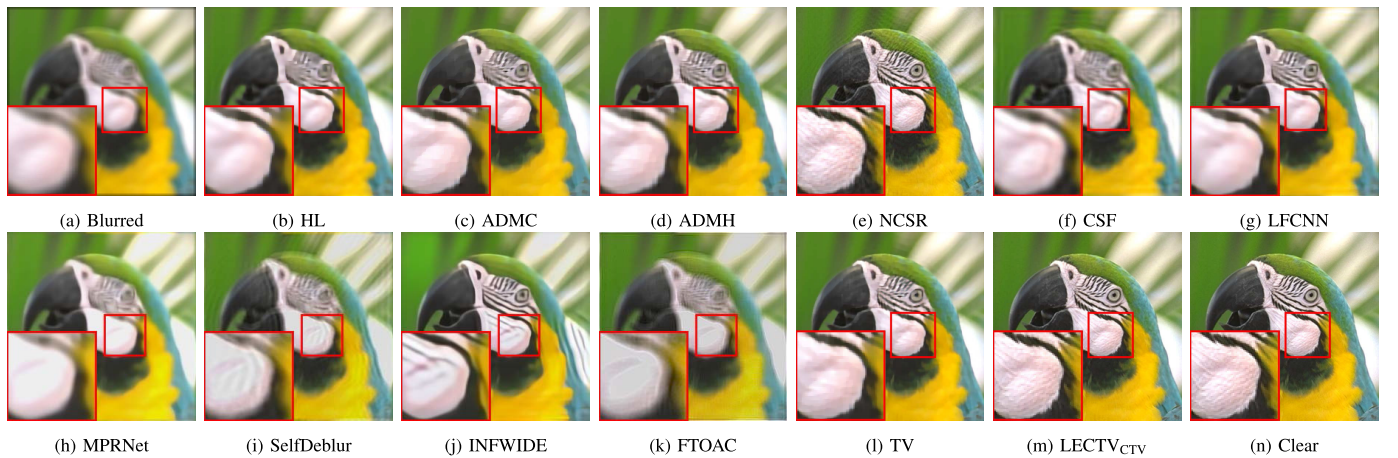
Fig. 8. Visual examples: SquareA.

WLRTR and OLRT reach the second and third rankings after LECTV in terms of quantification metrics values, but they spend more time than LECTV. According to Table IV, the time index (Time/s) of HL has an insightful advantage over others. Although the HL method for a single image takes the least time, its restoration result for HSI is not ideal, as observed by
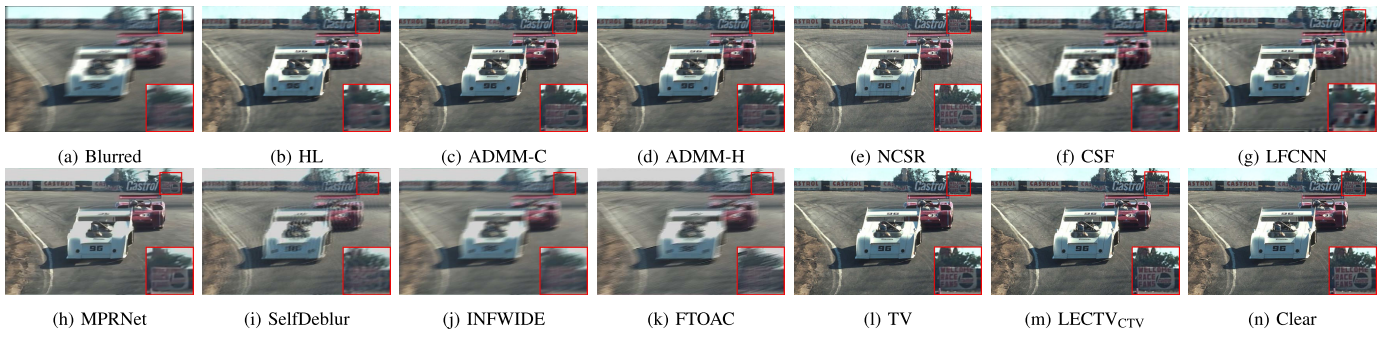
(a) Blurred   (b) HL   (c) ADMM-C   (d) ADMM-H   (e) NCSR   (f) CSF   (g) LFCNN

(h) MPRNet   (i) SelfDeblur   (j) INFWIDE   (k) FTOAC   (l) TV   (m) LECTV$_{CTV}$ (n) Clear

Fig. 9. Visual examples: MotionA.

TABLE IV
QUANTITATIVE EVALUATION RESULTS OF DIFFERENT METHODS ON CAVE DATASET

	Methods	HL	FPD	SSTV	WLRTR	OLRT	LECTV$_{CTV}$	LECTV$_{CHTV}$
Case A	PSNR	38.06	43.41	36.74	48.45	48.78	50.84	**50.89**
	SSIM	0.9535	0.9810	0.9490	0.9904	0.9904	0.9944	**0.9946**
	SAM	0.0657	0.0626	0.0699	0.0991	0.1025	0.0535	**0.0519**
	ERGAS	75.86	41.97	88.79	21.12	20.11	16.48	**16.03**
	Time/s	**5.86**	88.63	317.23	1129.20	854.84	540.45	700.50
Case B	PSNR	38.19	43.78	36.31	49.51	50.02	52.19	**52.30**
	SSIM	0.9523	0.9814	0.9459	0.9920	0.9926	0.9956	**0.9959**
	SAM	0.0901	0.0672	0.0647	0.0740	0.0909	0.0514	**0.0475**
	ERGAS	74.38	39.91	91.60	18.50	17.33	13.94	**13.50**
	Time/s	**5.72**	93.33	303.81	1124.33	848.98	580.10	625.21

(a) Blurred   (b) Restoration by LECTV$_{CTV}$

(c) Objective function   (d) PSNR
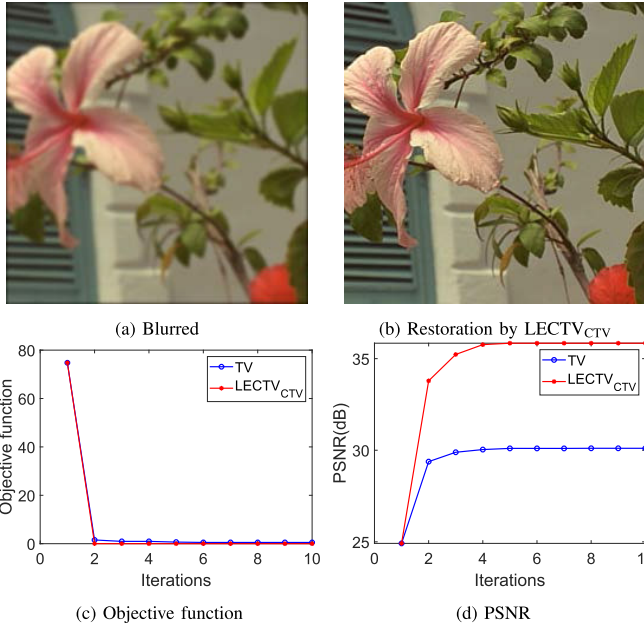
Fig. 10. Evolution of the objective function and PSNR value in the restoration process for TV and LECTV$_{CTV}$ on the flower image.

visual results in Fig. 11. Fig. 12 draws the specific PSNR and SSIM curves with respect to each band of 'fake and real strawberries' data. The SSIM and PSNR values based on the WLRTR, OLRT, and LECTV methods are all in the first echelon and overall higher than those of the HL, FPD, and

SSTV methods. Then, it is concluded that LECTV achieves the best results on PSNR and SSIM indexes for almost all bands. Further, it can be obtained from quantitative evaluations in Table IV that the average PSNR and SSIM values of LECTV is optimal are higher than those of WLRTR and OLRT.

Furthermore, from visual restoration results in Fig. 11, it gets that the HL cannot obtain satisfactory results for MSI restoration. Comparing to HL, SSTV and FPD are visually superior, but still do not have ideal restoration results. In contrast, WRLTR, OLRT, and the proposed LECTV exhibit better performance. And they can recover the detail information better and generate images with sharper edges and textures.

Fig. 13 shows spectral curves at spatial positions (326, 136) of 'chart and stuffed toy' data and (373, 64) of 'stuffed toys'. In particular, Fig. 13 plots the spectral curves between the restored spectrum with different methods and the original spectrum, where the Pearson correlation coefficients and Root Mean Square Error (RMSE) values are presented in the legend. Then, it evaluates the spectral curve in Fig. 13 with quantitative indices analysis. Table IV summaries the evaluation results on the spectral quality of the recovered HSI. It further verifies that LECTV can better restore the original spectrum by the spectral evaluation metrics SAM and ERGAS in Table IV. From Case A in Table IV, it follows that the LECTV$_{CTV}$ has the optimal result on SAM and the LECTV$_{CHTV}$ is evaluated to be highest on ERGAS. In Case B, LECTV$_{CHTV}$ and LECTV$_{CTV}$ obtain the optimal and sub-optimal values on SAM and ERGAS, respectively.
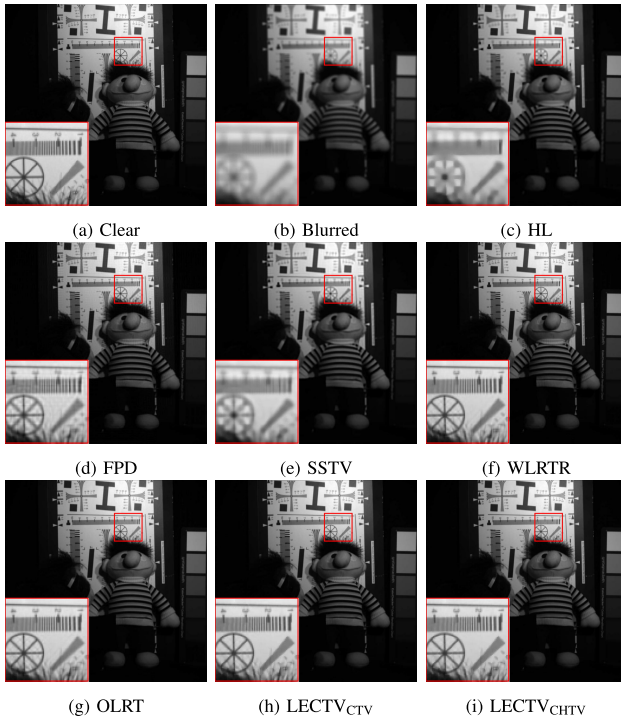
Fig. 11. Visual examples of restoration results on 'chart and stuffed toy' (band 24).
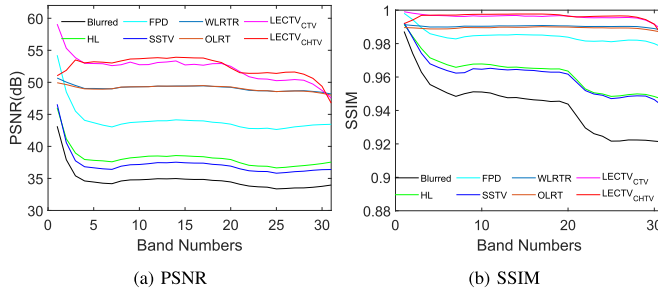
(a) Clear (b) Blurred (c) HL
(d) FPD (e) SSTV (f) WLRTR
(g) OLRT (h) LECTV$_{CTV}$ (i) LECTV$_{CHTV}$

(a) PSNR (b) SSIM

Fig. 12. PSNR and SSIM values of each band on 'fake and real strawberries' data (Case A).

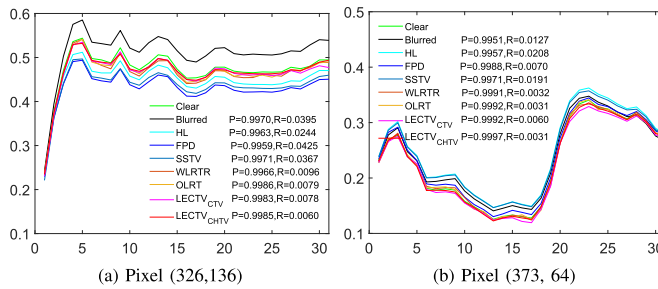(a) Pixel (326,136) (b) Pixel (373, 64)

Fig. 13. Spectral curves and their corresponding quantitative index with the original spectrum (a) position (326, 136) of 'chart and stuffed toy' in Case A; (b) position (373, 64) of 'stuffed toy' in Case A; 'P' and 'R' denote the pearson correlation coefficient and the root mean square error, respectively.

It further reflects that the proposed model can effectively recover the spectral information of HSI.

2) Experimental Results Analysis of HSI: Table V shows the evaluation results of seven methods on HSI datatset. As shown in Table V, LECTV$_{CHTV}$ have reached the best value on three quantitative metrics: PSNR, SSIM, and ERGAS, and
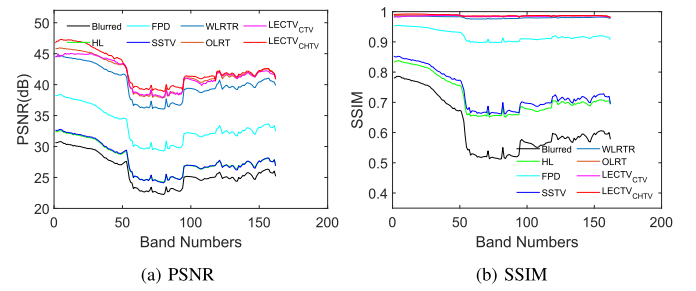

(a) PSNR (b) SSIM

Fig. 14. PSNR and SSIM values of each band on urban (Case A).

(a) Clear (b) Blurred (c) HL
(d) FPD (e) SSTV (f) WLRTR
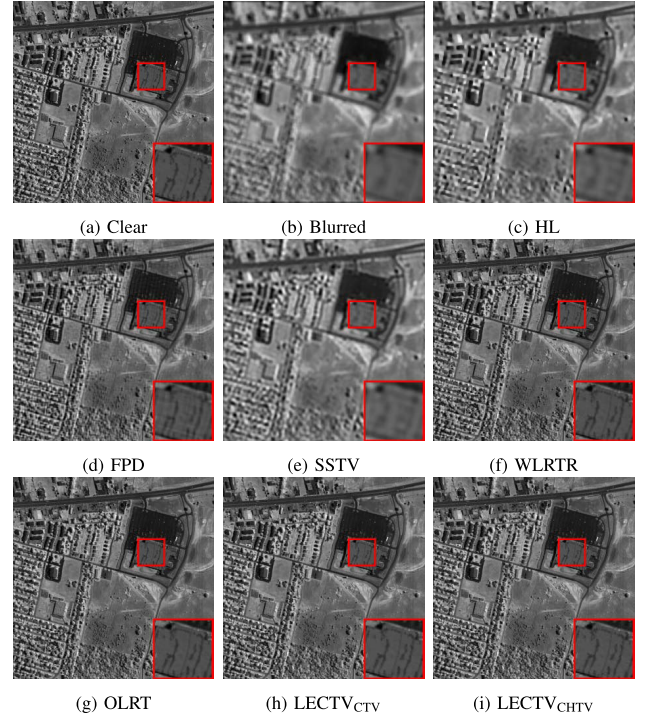(g) OLRT (h) LECTV$_{CTV}$ (i) LECTV$_{CHTV}$

Fig. 15. Visual examples of restoration result on urban.

the second-best SAM value. Fig. 14 draws the PSNR and SSIM values of the restoration results on each band of Urban data. It is observed that the curves of LECTV, WLRTR, and OLRT are in the first echelon and overall higher than those of FPD, SSTV, and HL. Specifically, the PSNR and SSIM values of LECTV$_{CHTV}$ reach the highest values in almost all bands, and LECTV$_{CTV}$ also displays excellent performance. In addition, it can be inferred from Time/s index in Table V that the LECTV takes less time than the tensor-based OLRT and WLRTR, which reflects the superiority of the proposed LECTV method.

Fig. 15 shows the visual results of different algorithms on Urban data. It can be seen that Figs. 15(h)-(i) have excellent visual quality with the proposed LECTV method. In contrast, the HL fails to produce a satisfactory result. Although the performances of SSTV and FPD are better than HL, they do still not have the ideal performance. Especially, there exist obvious ringing artifacts of FPD results at the edge positions from Fig. 15(d). In Fig. 15(e), it can be observed that the resulting SSTV has obvious blurring residues. Overall, WLRTR, OLRT, and LECTV are superior than HL, SSTV,

TABLE V

QUANTITATIVE EVALUATION RESULTS OF DIFFERENT METHODS ON HSI DATASET

	Methods	HL	FPD	SSTV	WLRTR	OLRT	LECTV$_{CTV}$	LECTV$_{CHTV}$
Case A	PSNR	28.42	33.16	28.59	40.52	42.01	42.19	**42.53**
	SSIM	0.7582	0.9209	0.7760	0.9799	0.9847	0.9853	**0.9863**
	SAM	0.0887	0.0608	0.0873	0.0399	**0.0365**	0.0390	0.0374
	ERGAS	153.31	88.84	150.50	38.34	32.35	31.53	**30.49**
	Time/s	**14.11**	176.69	622.91	2435.01	1739.05	1044.47	1401.42
Case B	PSNR	28.25	33.59	29.53	42.15	43.56	43.69	**44.14**
	SSIM	0.7474	0.9277	0.8046	0.9852	0.9887	0.9890	**0.9899**
	SAM	0.0909	0.0588	0.0812	0.0349	**0.0314**	0.0322	0.0318
	ERGAS	156.23	84.46	135.54	27.13	31.84	26.58	**25.44**
	Time/s	**13.95**	175.55	556.38	2455.69	1737.56	1235.61	1567.49

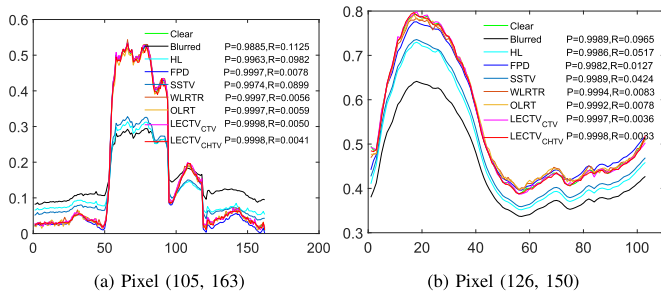(a) Pixel (105, 163) (b) Pixel (126, 150)

Fig. 16. Spectral curves and their corresponding quantitative index with the original spectrum. (a) position (105, 163) of Urban in Case A; (b) position (126, 150) of Pavia University in Case A; 'P' and 'R' represent the Pearson correlation coefficient and the Root Mean Square Error, respectively.

TABLE VI

PERFORMANCE OF MORE BLUR SCENES

Case	Index	Dataset1	Dataset1	Dataset3
Motion1	PSNR	29.99	31.26	31.26
	SSIM	0.8835	0.8684	0.8684
Motion2	PSNR	31.22	0.9141	32.63
	SSIM	0.9141	0.9050	0.9077
Motion3	PSNR	29.47	31.87	30.85
	SSIM	0.8909	0.9061	0.8743
Disk1	PSNR	25.77	26.96	28.31
	SSIM	0.7836	0.7816	0.8019

and FPD in terms of visual performance. They can effectively restore images and achieve better detail effects, visually. With comprehensive quantitative and qualitative evaluation, LECTV achieves satisfactory results on HSI deblurring.

Fig. 16 presents the spectral features at spatial positions (105, 163) of Urban and (126, 150) of Pavia University. From Fig. 16, we find that LECTV is closer to ground-truth (clear) than other competitors. It is obvious that the closer the recovery curve is to the original spectral curve, the better the quality of the recovery. Furthermore, a quantitative analysis of curves in Fig. 16 is conducted to calculate the Pearson correlation coefficient and RMSE attached in the legend of Fig. 16. The quantitative results also prove the superiority of our developed LECTV method, which is consistent with evaluation results in Table V. From Table V, LECTV$_{CHTV}$ achieves the best performance on ERGAS value and the second-best performance on SAM in Cases A and B. It shows the superiority of the proposed method in preserving spectral information. Compared with LECTV$_{CTV}$, the improved performance of LECTV$_{CHTV}$ in HSI experiments also indicates the effectiveness of LECTV$_{CHTV}$ in spectral compensation. Besides, LECTV$_{CHTV}$ also shows the optimal values in terms of PSNR and SSIM.

After conducting the aforementioned analysis, it is evident that the proposed LECTV method demonstrates superior performance, both visually and quantitatively. This indicates

that LECTV$_{CHTV}$ effectively leverages the advantages of prior knowledge regarding blurry images and the spatial-spectral TV model. The spatial-spectral TV model efficiently compensates for interfered information based on the spatial and spectral correlations of HSI, removing relatively heavier blur and noise in specific bands. Additionally, the per-pixel adaptive constraint further enhances compensation for detailed information. As a result, LECTV takes reliable performance in terms of recovering both spatial and spectral information.

E. Discussion

In previous subsections, experimental results have demonstrated the effectiveness and superiority of the proposed method in Gaussian blur, square blur, and simple motion blur. This subsection further discusses whether the proposed LECTV remains advantageous in more complex motion blur cases and defocus blur. Utilizing three motion blur kernels in [77], three experiments (Motion1, Motion2, and Motion3) are redesigned to evaluate the performance of our method in a wider range of scenarios, and the corresponding experiment results are listed in Table VI. From [1], the settings are selected for defocus blur, where a disk kernel, denoted as Disk1, with a radius of 5 is used for a simple simulation. In addition, we setup the noise level of 0.002 in each experiment to simulate the noise conditions. Table VI summaries the quantitative evaluation results. Fig. 17 showcases the restored visual

(a) Blurred (Motion1) (b) Ours/31.22dB

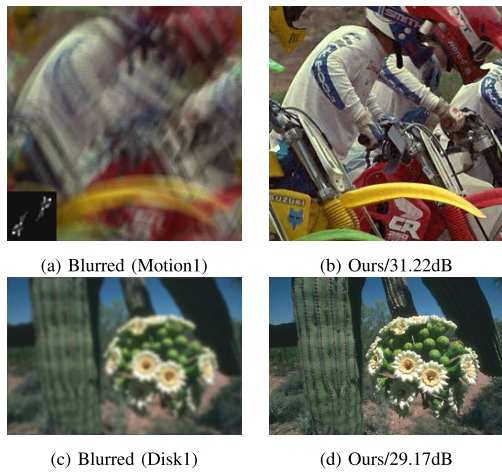(c) Blurred (Disk1) (d) Ours/29.17dB

Fig. 17. Illustration of the more blur results.

outcomes. According to Table VI and Fig. 17, we can conclude that the presented method displays the reliable and excellent performance under higher noise level and more complex blur scenes.

However, the aforementioned settings in practice do not accurately model the complex defocus blur. Since defocus blur typically involves the issue of focusing light in front of or behind the focal plane, it results in different focal points at different locations in the image. For spatially varying defocus blur in a certain scenario, it needs to match a specific processing method, such as the estimation of the depth map and blur kernel, etc., which will be also considered in our future work.

V. Conclusion

This paper developed a constrained TV model guided by blurred image priors for natural and hyperspectral image deblurring. In contrast to the existing DCP-based methods with only considering the overall sparse property of the image dark channel, our proposed method can adaptively characterize per-pixel of image. From experiments on natural and hyperspectral images, it finds that presented LECTV method is capable of adaptively recovering different texture regions in the image, including salient structure and detail information. It is also concluded that our method performs better after comparison analysis on both visual observations and quantitative evaluations. Nevertheless, there exist still some limitations of our method, which is not capable of dealing with images subject to strong random noise or stripe noise. For these problems, references [78] and [79] provide the modeling scheme for strip noise-disturbed images, and the deblurring method for noisy images, respectively. Inspired by [78] and [79], our future work will develop the improved LECTV method to further enhance the robustness and adaptation to noises. Besides, we hope to integrate our proposed model into the DL-based image deblurring method and extend it to subsequent tasks, such as classification and object detection.

References

[1] R. Wang and D. Tao, "Training very deep CNNs for general non-blind deconvolution," *IEEE Trans. Image Process.*, vol. 27, no. 6, pp. 2897–2910, Jun. 2018.

[2] B. Luo, Z. Cheng, L. Xu, G. Zhang, and H. Li, "Blind image deblurring via superpixel segmentation prior," *IEEE Trans. Circuits Syst. Video Technol.*, vol. 32, no. 3, pp. 1467–1482, Mar. 2022.

[3] Y. Bai, H. Jia, M. Jiang, X. Liu, X. Xie, and W. Gao, "Single-image blind deblurring using multi-scale latent structure prior," *IEEE Trans. Circuits Syst. Video Technol.*, vol. 30, no. 7, pp. 2033–2045, Jul. 2020.

[4] N. Wiener, N. Wiener, C. Mathematician, N. Wiener, N. Wiener, and C. Mathématicien, *Extrapolation, Interpolation, and Smoothing of Stationary Time Series: With Engineering Applications*, vol. 113, no. 21. Cambridge, MA, USA: MIT Press, 1949.

[5] W. H. Richardson, "Bayesian-based iterative method of image restoration," *J. Opt. Soc. Amer.*, vol. 62, no. 1, pp. 55–59, Jan. 1972.

[6] W. Ren, X. Cao, J. Pan, X. Guo, W. Zuo, and M.-H. Yang, "Image deblurring via enhanced low-rank prior," *IEEE Trans. Image Process.*, vol. 25, no. 7, pp. 3426–3437, Jul. 2016.

[7] A. Danielyan, V. Katkovnik, and K. Egiazarian, "BM3D frames and variational image deblurring," *IEEE Trans. Image Process.*, vol. 21, no. 4, pp. 1715–1728, Apr. 2012.

[8] H. Zhang, D. Wipf, and Y. Zhang, "Multi-image blind deblurring using a coupled adaptive sparse prior," in *Proc. IEEE Conf. Comput. Vis. Pattern Recognit.*, Jun. 2013, pp. 1051–1058.

[9] S. Liu, Y. Feng, S. Zhang, H. Song, and S. Chen, "L_0 sparse regularization-based image blind deblurring approach for solid waste image restoration," *IEEE Trans. Ind. Electron.*, vol. 66, no. 12, pp. 9837–9845, Dec. 2019.

[10] L. Sha, D. Schonfeld, and J. Wang, "Graph Laplacian regularization with sparse coding for image restoration and representation," *IEEE Trans. Circuits Syst. Video Technol.*, vol. 30, no. 7, pp. 2000–2014, Jul. 2020.

[11] Q. Zhang, Q. Yuan, M. Song, H. Yu, and L. Zhang, "Cooperated spectral low-rankness prior and deep spatial prior for HSI unsupervised denoising," *IEEE Trans. Image Process.*, vol. 31, pp. 6356–6368, 2022.

[12] J. Hao, J. Xue, Y. Zhao, and J. C. Chan, "Transformed structured sparsity with smoothness for hyperspectral image deblurring," *IEEE Geosci. Remote Sens. Lett.*, vol. 20, pp. 1–5, 2023.

[13] Q. Zhang, Y. Dong, Q. Yuan, M. Song, and H. Yu, "Combined deep priors with low-rank tensor factorization for hyperspectral image restoration," *IEEE Geosci. Remote Sens. Lett.*, vol. 20, pp. 1–5, 2023.

[14] L. Chen, F. Fang, T. Wang, and G. Zhang, "Blind image deblurring with local maximum gradient prior," in *Proc. IEEE/CVF Conf. Comput. Vis. Pattern Recognit. (CVPR)*, Jun. 2019, pp. 1742–1750.

[15] J. Pan, Z. Hu, Z. Su, and M.-H. Yang, "L_0-regularized intensity and gradient prior for deblurring text images and beyond," *IEEE Trans. Pattern Anal. Mach. Intell.*, vol. 39, no. 2, pp. 342–355, Feb. 2017.

[16] Q. Shan, J. Jia, and A. Agarwala, "High-quality motion deblurring from a single image," *ACM Trans. Graph.*, vol. 27, no. 3, pp. 1–10, Aug. 2008.

[17] J. Zhang, D. Zhao, R. Xiong, S. Ma, and W. Gao, "Image restoration using joint statistical modeling in a space-transform domain," *IEEE Trans. Circuits Syst. Video Technol.*, vol. 24, no. 6, pp. 915–928, Jun. 2014.

[18] W. Dong, L. Zhang, G. Shi, and X. Li, "Nonlocally centralized sparse representation for image restoration," *IEEE Trans. Image Process.*, vol. 22, no. 4, pp. 1620–1630, Apr. 2013.

[19] C.-C. Lee and W.-L. Hwang, "Sparse representation of a blur kernel for out-of-focus blind image restoration," in *Proc. IEEE Int. Conf. Image Process. (ICIP)*, Sep. 2016, pp. 2698–2702.

[20] W. Xu, Q. Zhu, N. Qi, and D. Chen, "Deep sparse representation based image restoration with denoising prior," *IEEE Trans. Circuits Syst. Video Technol.*, vol. 32, no. 10, pp. 6530–6542, Oct. 2022.

[21] J. M. Bioucas-Dias, M. A. T. Figueiredo, and J. P. Oliveira, "Total variation-based image deconvolution: A majorization-minimization approach," in *Proc. IEEE Int. Conf. Acoust. Speech Signal Process. Proc.*, vol. 2, May 2006, pp. II–II.

[22] S. Tang, W. Gong, W. Li, and W. Wang, "Non-blind image deblurring method by local and nonlocal total variation models," *Signal Process.*, vol. 94, pp. 339–349, Jan. 2014.

[23] D. Ren, H. Zhang, D. Zhang, and W. Zuo, "Fast total-variation based image restoration based on derivative alternated direction optimization methods," *Neurocomputing*, vol. 170, pp. 201–212, Dec. 2015.

[24] M. R. Chowdhury, J. Qin, and Y. Lou, "Non-blind and blind deconvolution under Poisson noise using fractional-order total variation," *J. Math. Imag. Vis.*, vol. 62, no. 9, pp. 1238–1255, Nov. 2020.

[25] J. P. Oliveira, J. M. Bioucas-Dias, and M. A. T. Figueiredo, "Adaptive total variation image deblurring: A majorization–minimization approach," *Signal Process.*, vol. 89, no. 9, pp. 1683–1693, 2009.

[26] Q. Zhang, Y. Zheng, Q. Yuan, M. Song, H. Yu, and Y. Xiao, "Hyperspectral image denoising: From model-driven, data-driven, to model-data-driven," *IEEE Trans. Neural Netw. Learn. Syst.*, 2023, doi: 10.1109/TNNLS.2023.3278866.

[27] H. Zeng, X. Xie, H. Cui, H. Yin, and J. Ning, "Hyperspectral image restoration via global L_{1-2} spatial–spectral total variation regularized local low-rank tensor recovery," *IEEE Trans. Geosci. Remote Sens.*, vol. 59, no. 4, pp. 3309–3325, Apr. 2021.

[28] T. Hu, W. Li, N. Liu, R. Tao, F. Zhang, and P. Scheunders, "Hyperspectral image restoration using adaptive anisotropy total variation and nuclear norms," *IEEE Trans. Geosci. Remote Sens.*, vol. 59, no. 2, pp. 1516–1533, Feb. 2021.

[29] Q. Zhang, Q. Yuan, J. Li, X. Liu, H. Shen, and L. Zhang, "Hybrid noise removal in hyperspectral imagery with a spatial–spectral gradient network," *IEEE Trans. Geosci. Remote Sens.*, vol. 57, no. 10, pp. 7317–7329, Oct. 2019.

[30] M. Wang, Q. Wang, J. Chanussot, and D. Hong, "L_0-L_1 hybrid total variation regularization and its applications on hyperspectral image mixed noise removal and compressed sensing," *IEEE Trans. Geosci. Remote Sens.*, vol. 59, no. 9, pp. 7695–7710, Sep. 2021.

[31] X. Fei, Z. Wei, and L. Xiao, "Iterative directional total variation refinement for compressive sensing image reconstruction," *IEEE Signal Process. Lett.*, vol. 20, no. 11, pp. 1070–1073, Nov. 2013.

[32] J. Qin, X. Yi, and S. Weiss, "A novel fluorescence microscopy image deconvolution approach," in *Proc. IEEE 15th Int. Symp. Biomed. Imag. (ISBI)*, Apr. 2018, pp. 441–444.

[33] O. V. Michailovich, "An iterative shrinkage approach to total-variation image restoration," *IEEE Trans. Image Process.*, vol. 20, no. 5, pp. 1281–1299, May 2011.

[34] C. Chen, M. K. Ng, and X.-L. Zhao, "Alternating direction method of multipliers for nonlinear image restoration problems," *IEEE Trans. Image Process.*, vol. 24, no. 1, pp. 33–43, Jan. 2015.

[35] B. Jiang and W. Lu, "Primal–dual optimization strategy with total variation regularization for prestack seismic image deblurring," *IEEE Trans. Geosci. Remote Sens.*, vol. 59, no. 1, pp. 884–893, Jan. 2021.

[36] J. Xie, G. Hou, G. Wang, and Z. Pan, "A variational framework for underwater image dehazing and deblurring," *IEEE Trans. Circuits Syst. Video Technol.*, vol. 32, no. 6, pp. 3514–3526, Jun. 2022.

[37] H. Fang, C. Luo, G. Zhou, and X. Wang, "Hyperspectral image deconvolution with a spectral–spatial total variation regularization," *Can. J. Remote Sens.*, vol. 43, no. 4, pp. 384–395, Jul. 2017.

[38] M. Chen, Y. Quan, Y. Xu, and H. Ji, "Self-supervised blind image deconvolution via deep generative ensemble learning," *IEEE Trans. Circuits Syst. Video Technol.*, vol. 33, no. 2, pp. 634–647, Feb. 2023.

[39] X. Tao, H. Gao, X. Shen, and J. Wang, "Scale-recurrent network for deep image deblurring," in *Proc. IEEE Conf. CVPR*, Jun. 2018, pp. 8174–8182.

[40] Y. Mao, Z. Wan, Y. Dai, and X. Yu, "Deep idempotent network for efficient single image blind deblurring," *IEEE Trans. Circuits Syst. Video Technol.*, vol. 33, no. 1, pp. 172–185, Jan. 2023.

[41] S. Xie, X. Zheng, W.-Z. Shao, Y.-D. Zhang, T. Lv, and H. Li, "Non-blind image deblurring method by the total variation deep network," *IEEE Access*, vol. 7, pp. 37536–37544, 2019.

[42] X. Zhang, T. Wang, R. Jiang, L. Zhao, and Y. Xu, "Multi-attention convolutional neural network for video deblurring," *IEEE Trans. Circuits Syst. Video Technol.*, vol. 32, no. 4, pp. 1986–1997, Apr. 2022.

[43] S. Wan et al., "Deep convolutional-neural-network-based channel attention for single image dynamic scene blind deblurring," *IEEE Trans. Circuits Syst. Video Technol.*, vol. 31, no. 8, pp. 2994–3009, Aug. 2021.

[44] H. S. Lee and S. I. Cho, "Locally adaptive channel attention-based spatial–spectral neural network for image deblurring," *IEEE Trans. Circuits Syst. Video Technol.*, vol. 33, no. 10, pp. 5375–5390, Oct. 2023.

[45] D. Ren, K. Zhang, Q. Wang, Q. Hu, and W. Zuo, "Neural blind deconvolution using deep priors," in *Proc. IEEE/CVF Conf. Comput. Vis. Pattern Recognit. (CVPR)*, Jun. 2020, pp. 3338–3347.

[46] S. W. Zamir et al., "Multi-stage progressive image restoration," in *Proc. IEEE/CVF Conf. Comput. Vis. Pattern Recognit. (CVPR)*, Jun. 2021, pp. 14821–14831.

[47] M. Chen, Y. Quan, T. Pang, and H. Ji, "Nonblind image deconvolution via leveraging model uncertainty in an untrained deep neural network," *Int. J. Comput. Vis.*, vol. 130, no. 7, pp. 1770–1789, Jul. 2022.

[48] K. He, J. Sun, and X. Tang, "Single image haze removal using dark channel prior," *IEEE Trans. Pattern Anal. Mach. Intell.*, vol. 33, no. 12, pp. 2341–2353, Dec. 2011.

[49] A. Golts, D. Freedman, and M. Elad, "Unsupervised single image dehazing using dark channel prior loss," *IEEE Trans. Image Process.*, vol. 29, pp. 2692–2701, 2020.

[50] Z. Li, J. Zheng, W. Yao, and Z. Zhu, "Single image haze removal via a simplified dark channel," in *Proc. IEEE Int. Conf. Acoust., Speech Signal Process. (ICASSP)*, Apr. 2015, pp. 1608–1612.

[51] C. Li, J. Quo, Y. Pang, S. Chen, and J. Wang, "Single underwater image restoration by blue-green channels dehazing and red channel correction," in *Proc. IEEE Int. Conf. Acoust., Speech Signal Process. (ICASSP)*, Mar. 2016, pp. 1731–1735.

[52] Y. Peng, K. Cao, and P. C. Cosman, "Generalization of the dark channel prior for single image restoration," *IEEE Trans. Image Process.*, vol. 27, no. 6, pp. 2856–2868, Jun. 2018.

[53] J. Pan, D. Sun, H. Pfister, and M. Yang, "Deblurring images via dark channel prior," *IEEE Trans. Pattern Anal. Mach. Intell.*, vol. 40, no. 10, pp. 2315–2328, Oct. 2018.

[54] X. Ge, J. Tan, and L. Zhang, "Blind image deblurring using a non-linear channel prior based on dark and bright channels," *IEEE Trans. Image Process.*, vol. 30, pp. 6970–6984, 2021.

[55] F. Wen, R. Ying, Y. Liu, P. Liu, and T.-K. Truong, "A simple local minimal intensity prior and an improved algorithm for blind image deblurring," *IEEE Trans. Circuits Syst. Video Technol.*, vol. 31, no. 8, pp. 2923–2937, Aug. 2021.

[56] Y. Yan, W. Ren, Y. Guo, R. Wang, and X. Cao, "Image deblurring via extreme channels prior," in *Proc. IEEE Conf. Comput. Vis. Pattern Recognit. (CVPR)*, Jul. 2017, pp. 6978–6986.

[57] H. Lim, S. Yu, K. Park, D. Seo, and J. Paik, "Texture-aware deblurring for remote sensing images using ℓ_0-based deblurring and ℓ_2-based fusion," *IEEE J. Sel. Topics Appl. Earth Observ. Remote Sens.*, vol. 13, pp. 3094–3108, 2020.

[58] S. Cao, W. Tan, K. Xing, H. He, and J. Jiang, "Dark channel inspired deblurring method for remote sensing image," *J. Appl. Remote Sens.*, vol. 12, no. 1, 2018, Art. no. 015012.

[59] Q. Yuan, L. Zhang, and H. Shen, "Hyperspectral image denoising employing a spectral–spatial adaptive total variation model," *IEEE Trans. Geosci. Remote Sens.*, vol. 50, no. 10, pp. 3660–3677, Oct. 2012.

[60] X. Zheng, Y. Yuan, and X. Lu, "Hyperspectral image denoising by fusing the selected related bands," *IEEE Trans. Geosci. Remote Sens.*, vol. 57, no. 5, pp. 2596–2609, May 2019.

[61] H. Liu, R. Xiong, D. Liu, S. Ma, F. Wu, and W. Gao, "Image denoising via low rank regularization exploiting intra and inter patch correlation," *IEEE Trans. Circuits Syst. Video Technol.*, vol. 28, no. 12, pp. 3321–3332, Dec. 2018.

[62] C. Yi, Y.-Q. Zhao, and J. C. Chan, "Hyperspectral image super-resolution based on spatial and spectral correlation fusion," *IEEE Trans. Geosci. Remote Sens.*, vol. 56, no. 7, pp. 4165–4177, Jul. 2018.

[63] L. I. Rudin, S. Osher, and E. Fatemi, "Nonlinear total variation based noise removal algorithms," *Phys. D, Nonlinear Phenomena*, vol. 60, nos. 1–4, pp. 259–268, 1992.

[64] Y. Chang, L. Yan, H. Fang, and C. Luo, "Anisotropic spectral–spatial total variation model for multispectral remote sensing image destriping," *IEEE Trans. Image Process.*, vol. 24, no. 6, pp. 1852–1866, Jun. 2015.

[65] R. M. Rameshan, S. Chaudhuri, and R. Velmurugan, "High dynamic range imaging under noisy observations," in *Proc. 18th IEEE Int. Conf. Image Process.*, Sep. 2011, pp. 1333–1336.

[66] U. Schmidt and S. Roth, "Shrinkage fields for effective image restoration," in *Proc. IEEE Conf. Comput. Vis. Pattern Recognit.*, Jun. 2014, pp. 2774–2781.

[67] N. Wang, W. Shi, C. Fan, and L. Zou, "An improved nonlocal sparse regularization-based image deblurring via novel similarity criteria," *Int. J. Adv. Robotic Syst.*, vol. 15, no. 3, May 2018, Art. no. 172988141878311.

[68] W. Ren et al., "Deep non-blind deconvolution via generalized low-rank approximation," in *Proc. Adv. Neural Inf. Process. Syst. (NIPS)*, vol. 31, 2018, pp. 295–305.

[69] D. Krishnan and R. Fergus, "Fast image deconvolution using hyper-Laplacian priors," in *Proc. Adv. Neural Inf. Process. Syst.*, vol. 22, 2009, pp. 1–9.

[70] J. Zhang, J. Pan, W. Lai, R. W. H. Lau, and M. Yang, "Learning fully convolutional networks for iterative non-blind deconvolution," in *Proc. IEEE Conf. Comput. Vis. Pattern Recognit. (CVPR)*, Jul. 2017, pp. 6969–6977.

[71] T. Eboli, J.-M. Morel, and G. Facciolo, "Fast two-step blind optical aberration correction," in *Proc. Eur. Conf. Comput. Vis. (ECCV)*. Berlin, Germany: Springer-Verlag, 2022, pp. 693–708.

[72] Z. Zhang, Y. Cheng, J. Suo, L. Bian, and Q. Dai, "INFWIDE: Image and feature space Wiener deconvolution network for non-blind image deblurring in low-light conditions," *IEEE Trans. Image Process.*, vol. 32, pp. 1390–1402, 2023.

[73] S. Henrot, C. Soussen, and D. Brie, "Fast positive deconvolution of hyperspectral images," *IEEE Trans. Image Process.*, vol. 22, no. 2, pp. 828–833, Feb. 2013.

[74] Y. Chang, L. Yan, X.-L. Zhao, H. Fang, Z. Zhang, and S. Zhong, "Weighted low-rank tensor recovery for hyperspectral image restoration," *IEEE Trans. Cybern.*, vol. 50, no. 11, pp. 4558–4572, Nov. 2020.

[75] Y. Chang, L. Yan, B. Chen, S. Zhong, and Y. Tian, "Hyperspectral image restoration: Where does the low-rank property exist," *IEEE Trans. Geosci. Remote Sens.*, vol. 59, no. 8, pp. 6869–6884, Aug. 2021.

[76] P. Wang et al., "Poissonian blurred hyperspectral imagery denoising based on variable splitting and penalty technique," *IEEE Trans. Geosci. Remote Sens.*, vol. 61, 2023, Art. no. 5505414.

[77] A. Levin, Y. Weiss, F. Durand, and W. T. Freeman, "Understanding and evaluating blind deconvolution algorithms," in *Proc. IEEE Conf. Comput. Vis. Pattern Recognit.*, Jun. 2009, pp. 1964–1971.

[78] S. Cao, H. Fang, L. Chen, W. Zhang, Y. Chang, and L. Yan, "Robust blind deblurring under stripe noise for remote sensing images," *IEEE Trans. Geosci. Remote Sens.*, vol. 60, 2022, Art. no. 5412117.

[79] M. Chen, Y. Chang, S. Cao, and L. Yan, "Learning blind denoising network for noisy image deblurring," in *Proc. IEEE Int. Conf. Acoust., Speech Signal Process. (ICASSP)*, May 2020, pp. 2533–2537.

Lan Li received the B.S. degree in software engineering from the Chaohu University, Chaohu, China, in 2018, and the M.S. degree in computer technology from Dalian Maritime University, Dalian, China, in 2021, where she is currently pursuing the Ph.D. degree with the School of Information Science and Technology.

From 2024 to 2025, She is a Visiting Research Scholar with the School of Information and Communication Technology, Griffith University, Nathan, QLD, Australia. Her research interests include remote sensing information processing.

Meiping Song (Member, IEEE) received the Ph.D. degree from the College of Computer Science and Technology, Harbin Engineering University, Harbin, China, in 2006.

From 2013 to 2014, she was a Visiting Assistant Researcher with the University of Maryland, College Park, MD, USA. She is currently a Professor with the College of Information Science and Technology, Dalian Maritime University, Dalian, China. Her research interests include remote sensing and hyperspectral image processing.

Qiang Zhang (Member, IEEE) received the B.E. degree in surveying and mapping engineering and the M.E. and Ph.D. degrees in photogrammetry and remote sensing from Wuhan University, Wuhan, China, in 2017, 2019, and 2022, respectively.

He is currently a Xinghai Associate Professor with the Center of Hyperspectral Imaging in Remote Sensing, College of Information Science and Technology, Dalian Maritime University, Dalian, China. He has published more than ten journal articles on IEEE TRANSACTIONS ON IMAGE PROCESSING, IEEE TRANSACTIONS ON NEURAL NETWORKS AND LEARNING SYSTEMS, IEEE TRANSACTIONS ON GEOSCIENCE AND REMOTE SENSING, and *ISPRS Journal of Photogrammetry and Remote Sensing*. His research interests include remote sensing information processing, computer vision, and machine learning. More details could be found at https://qzhang95.github.io.

Yushuai Dong received the B.S. degree in food science and engineering from Huazhong Agricultural University, Wuhan, China, in 2022. He is currently pursuing the M.S. degree with the Information Science and Technology College, Dalian Maritime University, Dalian, China.

His research interests include hyperspectral image processing and machine learning.

Yulei Wang (Member, IEEE) was born in Yantai, Shandong, China, in 1986. She received the B.S. and Ph.D. degrees in signal and information processing from Harbin Engineering University, Harbin, China, in 2009 and 2015, respectively.

She is currently an Associate Professor and a Doctoral Supervisor with the Center for Hyperspectral Imaging in Remote Sensing (CHIRS), Information Science and Technology College, Dalian Maritime University, Dalian, China. Her research interests include hyperspectral image (HSI) processing and vital signs signal processing.

Dr. Wang was awarded by the China Scholarship Council in 2011 as a Joint Ph.D. Student to study at the Remote Sensing Signal and Image Processing Laboratory, University of Maryland, Baltimore County, Baltimore, MD, USA, for two years.

Qiangqiang Yuan (Member, IEEE) received the B.S. degree in surveying and mapping engineering and the Ph.D. degree in photogrammetry and remote sensing from Wuhan University, Wuhan, China, in 2006 and 2012, respectively.

In 2012, he joined the School of Geodesy and Geomatics, Wuhan University, where he is currently a Professor. He has authored or coauthored more than 90 research articles, including more than 70 peer-reviewed articles in international journals, such as *Remote Sensing of Environment*, *ISPRS Journal of Photogrammetry and Remote Sensing*, IEEE TRANSACTIONS ON IMAGE PROCESSING, and IEEE TRANSACTIONS ON GEOSCIENCE AND REMOTE SENSING. His research interests include image reconstruction, remote sensing image processing and application, and data fusion.

Dr. Yuan was a recipient of the Youth Talent Support Program of China in 2019, the Top-Ten Academic Star of Wuhan University in 2011, and the Recognition of Best Reviewers of IEEE GEOSCIENCE AND REMOTE SENSING LETTERS in 2019. In 2014, he received the Hong Kong Scholar Award from the Society of Hong Kong Scholars and China National Postdoctoral Council. He is an associate editor of five international journals and he has frequently served as a referee for more than 40 international journals for remote sensing and image processing.